Opto-Electronic Advances

Article

March 2024, Vol. 7, No. 3

DOI: 10.29026/oea.2024.230178

Breaking the optical efficiency limit of virtual reality with a nonreciprocal polarization rotator

Yuqiang Ding[1], Zhenyi Luo[1], Garimagai Borjigin[1,2,3] and Shin-Tson Wu[1]*

A catadioptric lens structure, also known as pancake lens, has been widely used in virtual reality (VR) displays to reduce the formfactor. However, the utilization of a half mirror (HM) to fold the optical path thrice leads to a significant optical loss. The theoretical maximum optical efficiency is merely 25%. To transcend this optical efficiency constraint while retaining the foldable characteristic inherent to traditional pancake optics, in this paper, we propose a theoretically lossless folded optical system to replace the HM with a nonreciprocal polarization rotator. In our feasibility demonstration experiment, we used a commercial Faraday rotator (FR) and reflective polarizers to replace the lossy HM. The theoretically predicted 100% efficiency can be achieved approximately by using two high-extinction-ratio reflective polarizers. In addition, we evaluated the ghost images using a micro-OLED panel in our imaging system. Indeed, the ghost images can be suppressed to undetectable level if the optics are with antireflection coating. Our novel pancake optical system holds great potential for revolutionizing next-generation VR displays with lightweight, compact formfactor, and low power consumption.

Keywords: near-eye display; virtual reality; pancake optics; folded optics; nonreciprocal polarization rotator

Ding YQ, Luo ZY, Borjigin G et al. Breaking the optical efficiency limit of virtual reality with a nonreciprocal polarization rotator. *Opto-Electron Adv* **7**, 230178 (2024).

Introduction

Augmented reality (AR) and virtual reality (VR) have expanded our perceptual horizons and ushered in deeper human-digital interactions that transcend the confines of traditional flat panel displays. This evolution has unlocked a realm of exciting new possibilities, encompassing the metaverse, digital twins, and spatial computing, all of which have found widespread applications in diverse fields such as smart education and training, healthcare, navigation, gaming, entertainment, and smart manufacturing.

For AR and VR to become truly wearable for an extended period, there is a pressing need for compact and stylish formfactor, lightweight, and low power consumption. To achieve these objectives, extensive efforts have been devoted to designing novel optical elements and headset configurations[1–10]. Among these endeavors, polarization-based folded optics, often referred to as catadioptric or pancake optics, has emerged as a pivotal breakthrough for compact and lightweight VR headsets, such as Apple Vision Pro and Meta Quest Pro, etc.[11–14]. Figure 1(a) shows the device configuration of a conventional pancake optics system along with its essential components. Such a pancake optics not only delivers an exceptional image quality[15] but also offers an appealing formfactor. By folding the light path three times within the cavity,

[1]College of Optics and Photonics, University of Central Florida, Orlando FL 32816, USA; [2]Department of Intelligent Interaction Technologies, University of Tsukuba, Tsukuba, Ibaraki 305-8573, Japan; [3]Research Fellow of Japan Society for the Promotion of Science, Chiyoda-ku, Tokyo 102-0083, Japan.

*Correspondence: ST Wu, E-mail: swu@creol.ucf.edu

Received: 28 September 2023; Accepted: 25 December 2023; Published online: 26 January 2024

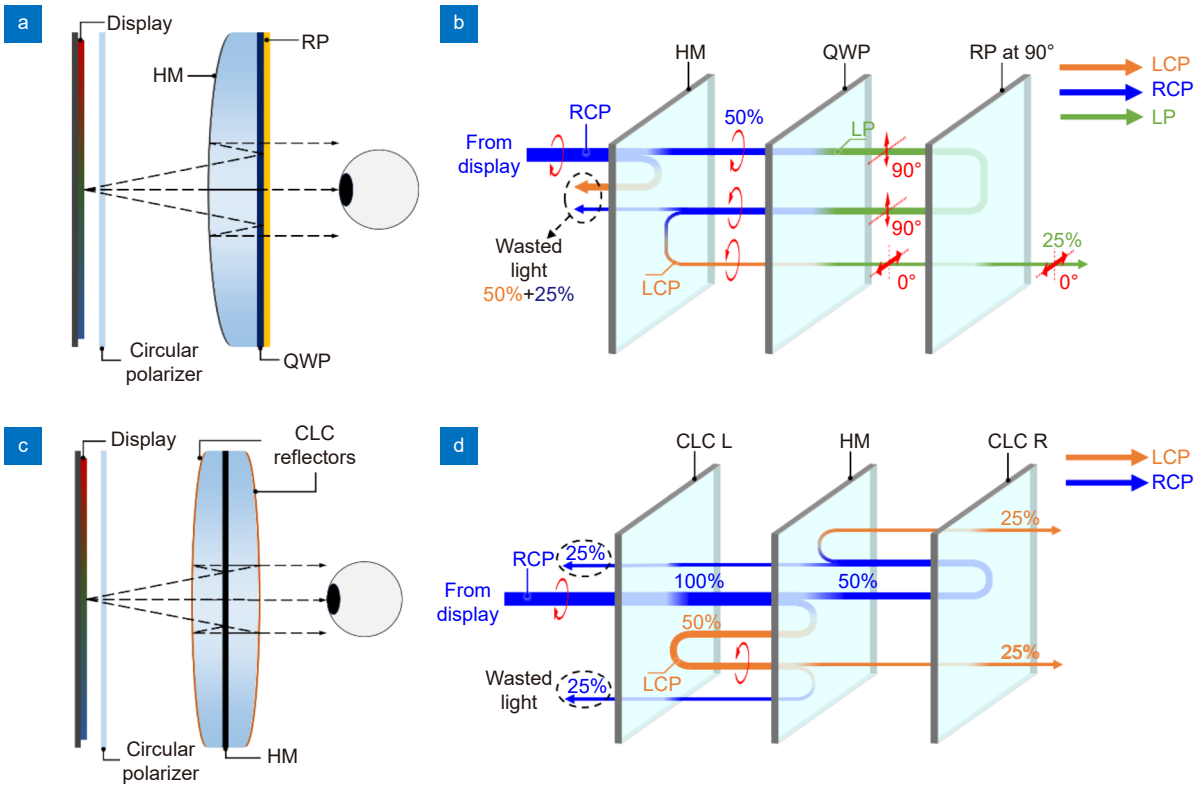

Fig. 1 | Concept of pancake optics systems. (**a**) Device configuration and (**b**) operation mechanism of conventional pancake optics system. (**c**) Configuration and (**d**) operation mechanism of double path pancake optics system. LCP, RCP, and LP represent left-handed circular polarization, right-handed circular polarization, and linear polarization.

these systems attain a shorter focal length, resulting in a significantly reduced volume. However, there is an inherent fundamental limit in this approach, a serious light loss. As depicted in Fig. 1(b), the emitted light from the microdisplay panel, e.g., liquid crystal display (LCD), keeps the following path: It goes through the HM, where 50% of the incident light is reflected and lost. The remaining 50% continues to the quarter-wave plate (QWP) and the reflective polarizer (RP), where almost all the light is reflected to the HM. Another 25% passing through the HM, results in additional loss. Ultimately, only about 25% of the light (assuming no other loss) from the display panel reaches the observer's eye. However, if the display emits an unpolarized light, then the maximum optical efficiency is further reduced to 12.5%.

As modern wireless AR and VR headsets are powered by batteries, such a low light efficiency imposes a significant challenge, limiting the continuous operation time to about two hours. To overcome this issue, some strategies have been attempted. From display side, collimated backlighting[16–18] and high aspect ratio with pixel optimization improve the light efficiency[19]. Another approach is to use a hologram film and laser sources[20]. From the pancake optics side, an innovative pancake optics design, called double path pancake optics, sandwiches the HM between two cholesteric liquid crystal (CLC) reflectors[21] or two pairs of RPs and QWPs[22], to double the efficiency as illustrated in Fig. 1(c, d). Nevertheless, the lens design must be symmetric with respect to the HM, which increases the volume of the pancake lens, and significantly decreases the design freedom, especially for the multiple-piece pancake lens. Moreover, this design still incurs at least 50% light loss due to the presence of the HM.

To eliminate the fundamental drawback caused by the HM and maintain a high degree of design freedom, in this paper, we propose a theoretically lossless pancake optics solution that incorporates a nonreciprocal polarization rotator sandwiched between two reflective polarizers. To prove concept, we conducted a preliminary experiment using commercially available components. Both total efficiency and ghost images are analyzed. The measured results agree with the theoretical analyses. Finally, the challenges of desired magnetic-optic materials are also discussed.

Working principles

Before introducing our new pancake system, it is essential to understand the concepts of reciprocal and nonreciprocal polarization rotations[23,24]. Optical rotation of a linearly polarized light, when passing through a material, results from the dispersion between the left-handed and right-handed circularly polarized (LCP and RCP) components. This dispersion, arising from the chirality or handedness in the crystal structure or constituent molecules, is referred to as natural optical activity. When a chirality or handedness is induced by a magnetic field along the wave propagation direction, it is known as Faraday rotation.

In an optically active rotator, such as a half-wave plate, polarization rotation reverses when the propagation direction is reversed, as illustrated in Fig. 2(a, b). This phenomenon is called reciprocal polarization rotation. Consequently, after a roundtrip of forward and backward propagations, the initial polarization state is reproduced with no net rotation. In contrast to optical activity, the Faraday rotation angle θ is directly proportional to the magnetic field and the rotation direction is solely determined by the magnetic field, irrespective of the optical wave's propagation direction, as follows:

$$\theta(\lambda) = V(\lambda) BL\,, \tag{1}$$

where $V(\lambda)$ denotes the Verdet constant of the material, B represents the magnetic flux density in the propagation direction, and L stands for the length of the magneto-optical element. In Eq. (1), the magnetic flux density can be generated by a solenoid, external magnets, or the material itself (bias-magnet-free FR). As depicted in Fig. 2(c, d), the sense of polarization rotation is maintained when the propagation direction reverses, which is referred to as nonreciprocal polarization rotation. Consequently, a roundtrip of forward and backward propagation results in a net rotation of 2θ.

In the following, we introduce a novel pancake optics structure using the nonreciprocal polarization rotator described above. The system configuration is illustrated in Fig. 3(a). Our proposed pancake optics consists of a 45° FR sandwiched between two RPs with transmission axes inclined at 45° to each other. Here, this diagram solely illustrates the optical path with polarization and does not depict any bending power inside the pancake system. In an ideal scenario, a linearly polarized light, such as a horizontally polarized light from the microdisplay, initially passes through the first RP completely. It then impinges on the FR, transmitting through it and undergoing a 45° polarization rotation. The light is then reflected by the second RP and travels backward to the FR due to the polarization selectivity of the RP. Subsequently, all the light passes through the FR, experiencing another 45° polarization rotation and becoming vertically polarized. Under such condition, the light is reflected by the first RP and returns to the FR. It once again transmits through the FR and undergoes a 45° polarization rotation. Finally, all the light traverses through the second RP and reaches the user's eye. Throughout this entire process, there is no light loss because all the polarization rotations are achieved by the lossless FR. Additionally, a lens can be inserted at any position, eliminating the need for a symmetric lens design in the above-mentioned double path pancake system. For

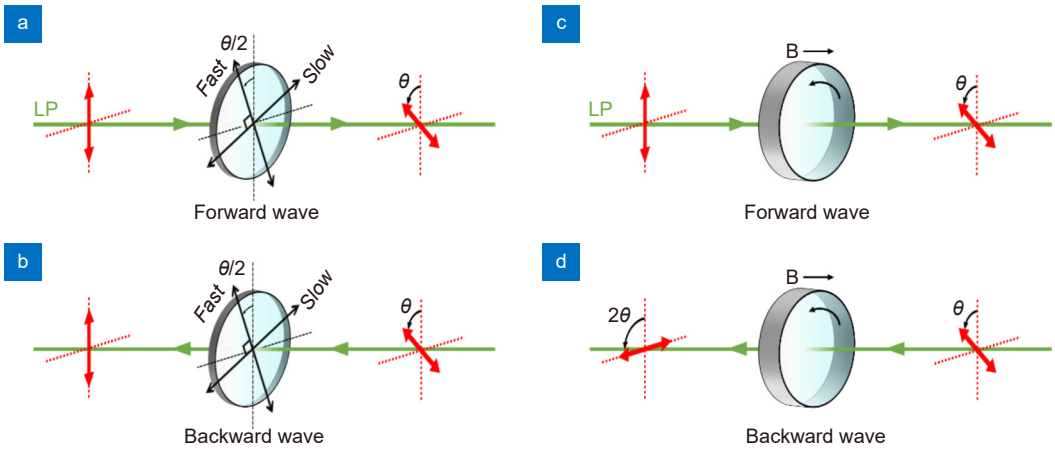

Fig. 2 | Schematic of reciprocal and nonreciprocal polarization rotators. Polarization rotation in (**a**) a reciprocal polarization rotator during forward propagation and (**b**) backward propagation. Polarization rotation in (**c**) a nonreciprocal polarization rotator through forward propagation and (**d**) backward propagation.

example, the lens can be inserted into the positions between the first RP and the FR or/and the FR and the second RP as shown in Fig. 2(b), where the lens curvature at the edge surfaces can be different.

Results and discussion

To prove concept, here we use a commercially available terbium gallium garnet (TGG) crystal as the Faraday rotator because of its large Verdet constant and low absorption in the visible spectral region, and two dual brightness enhancement films (DBEFs) as the reflective polarizers. Wire-grid polarizer is another RP candidate. To gain a better understanding of the polarization conversion process in our proposed pancake optics system, we constructed two folded systems: one with FR and another without, as depicted in Fig. 3(b). Firstly, to validate the optical efficiency in our system, we employed a 45° FR operating at 510–550 nm (from Thorlabs). A 532 nm laser is positioned at 4 cm in front of the first RP, and the laser beam is converted to horizontally polarized light using a linear polarizer. The distance between the two RPs is 5 cm. We intentionally enlarge the system volume for easier evaluation of different folded images, and the light source is inclined at a small angle for this purpose.

Figure 4 depicts the beams captured in the two folded optics systems. In Fig. 4(a), we can observe multiple folded beams (with five beams captured) in the optical system without the FR. In principle, there could be an infinite number of folded beams if the camera's dynamic range is high enough and the diameter of the RPs is sufficiently large. Due to the absence of polarization rotation, when the light encounters a RP, 50% of the light passes through, while the remaining 50% is reflected and continues this process. Based on the number of folds, we label these beams as 0th, 1st, 2nd, and so on, up to the nth orders. It is worth noting that as the number of folds increases, the efficiency decreases. Therefore, in Fig. 4(a), the beams are clearly distinguished as 0th, 1st, 2nd, 3rd, and 4th order from left to right.

Once we insert the FR into the folded system, our proposed pancake system is realized. Notably, the 1st-order folded beam becomes significantly brighter, while all other orders are almost vanished, indicating that the energy is primarily concentrated in the 1st-order folded beam, as Fig. 4(b) shows. Table 1 summarizes the normalized efficiency of each order in the two folded systems, and the data closely aligns with the theoretical efficiency shown in Fig. 4(a) and 4(b). Based on the data in

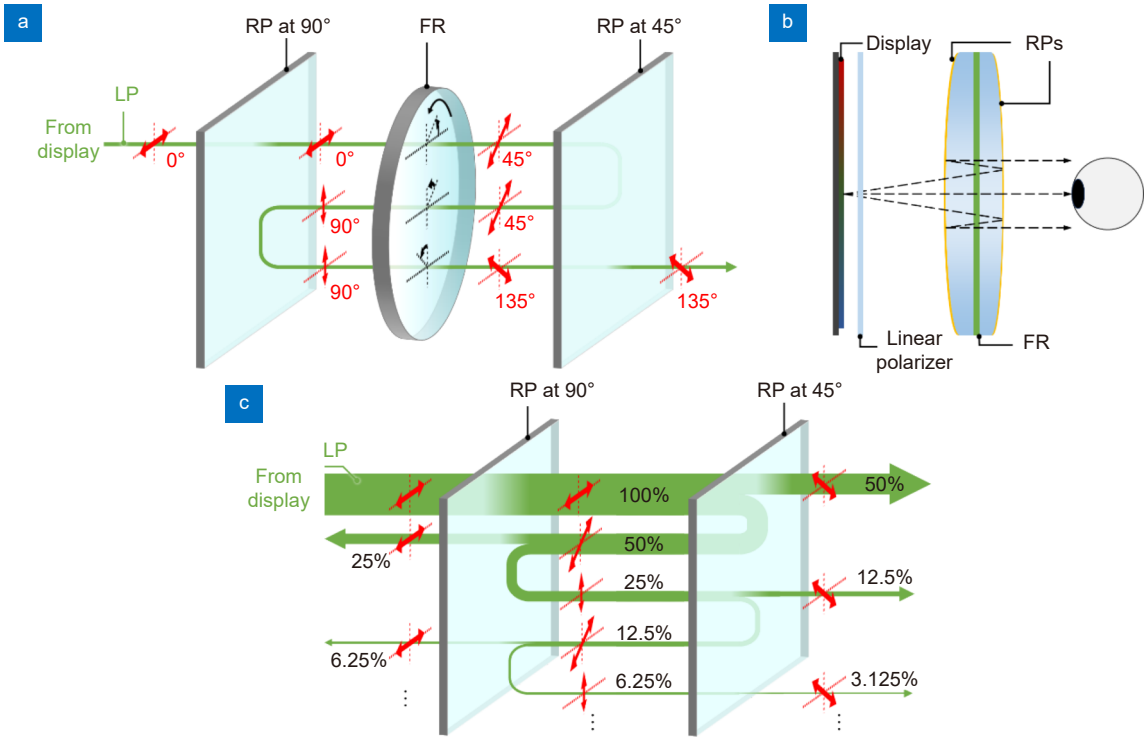

Fig. 3 | Working principle of the proposed novel pancake optics system. (**a**) Polarization conversion process in the proposed novel pancake optic system with a FR. (**b**) A possible configuration of the proposed novel pancake optics. (**c**) Polarization conversion process in the proposed novel pancake optic system without a FR.

Table 1, our pancake optics system achieves an optical efficiency of 71.5%. Later, we will explain why we do not get the theoretical 100% efficiency because of the imperfect optical components employed.

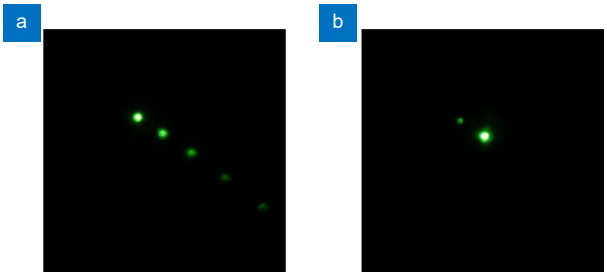

Fig. 4 | Experiments using a laser source. The folded beams in pancake optics system (**a**) without FR, (**b**) with FR.

While the optical efficiency of our proposed pancake system surpasses previous designs, it does not reach the expected theoretical limit, which is 100%. To analyze the energy loss, we need to consider the performance of all the optical elements. First, for the DBEF RPs in the green band (510–550 nm), the reflectance and transmittance in the block state is approximately 99% and 1%, while in the pass state is 1% and 99%, respectively. However, when the DBEF RPs are laminated on a glass substrate which has no antireflection coating, the reflectance and transmittance become 98.4% and 1.6% in the block state, and 8.5% and 91.5% in the pass state, respectively. This significantly reduces the overall optical efficiency because the folded image is reflected by the RPs twice and passing through the RPs twice.

Another critical optical element is the Faraday rotator, which is used to control the polarization rotation. Therefore, both transmission and polarization rotation ability are essential for analyzing the optical efficiency and ghost images. Using the FR operating at 510–550 nm as an example, its transmission spectrum is shown in Fig. 5(a). According to Thorlabs' specifications, the absorption of the FR is approximately 1%, while the reflectance and transmittance is about 1% and 98% at 532 nm, respectively. This also reduces the optical efficiency due to thrice polarization rotations in the FR. To measure the polarization rotation ability in the visible region, we sandwiched the FR between two absorptive linear polarizers oriented at 45° to each other, as depicted in Fig. 5(b). The measured spectrum is shown in Fig. 5(c), which closely aligns with the theoretical prediction (dashed lines)[25].

Overall, the optical efficiency is about 76.3% based on the parameters mentioned above. It is still a little bit higher than our measured optical efficiency, 71.5%. This ~5% difference may be attributed to the diffraction of the laser beam. By applying an antireflection coating (<0.25%) on the substrate, and employing a high-performance RP film like 3M™ RPs[15], which has 99.9% transmittance in the pass state and 99.9% reflectance in the block state, the optical efficiency can be significantly improved to 93.2%, which is ~4× higher than the conventional pancake lens.

In addition to the above-mentioned laser projector, we also investigated our pancake systems with a micro-OLED (organic light-emitting diode) panel, which has a wider spectrum. Figure 6 depicts the images captured in the two folded optics systems. Figure 6(a) shows the original image from the display panel. Multiple folded images in the optics system without the FR are displayed in Fig. 6(b, c), where two images (0^{th} and 1^{st} orders) were captured at different focal lengths. The larger image in Fig. 6(b) represents the 0^{th} order, while the smaller one in Fig. 6(c) represents the 1^{st} order. Upon inserting the FR into the folded system, the 1^{st} order folded image becomes much brighter, indicating that the energy is primarily concentrated in the 1^{st} order folded image, as shown in Fig. 6(d). Furthermore, we implemented the same folded optics systems with a FR operating in the red band (603–663 nm). All the captured images are presented in Fig. 6(e–h).

Similar to traditional pancake optics systems[13,26,27], it is evident that our proposed design also suffers from ghost images as Fig. 6(d) and 6(h) show. In the following sections, we will analyze the causes of different types of ghost images and provide corresponding methods to suppress or eliminate them.

The first type of ghost images arises from the leaked transmission of the RPs in the block state, which is around 1.6%. As depicted in Fig. 7(a), approximately

Table 1 | Summary of the optical efficiency in two folded optics systems.

Folded optics system	0^{th}	1^{st}	2^{nd}
W/O Faraday rotator	44.7%	9.7%	2.4%
W/ Faraday rotator	2.3%	71.5%	0%

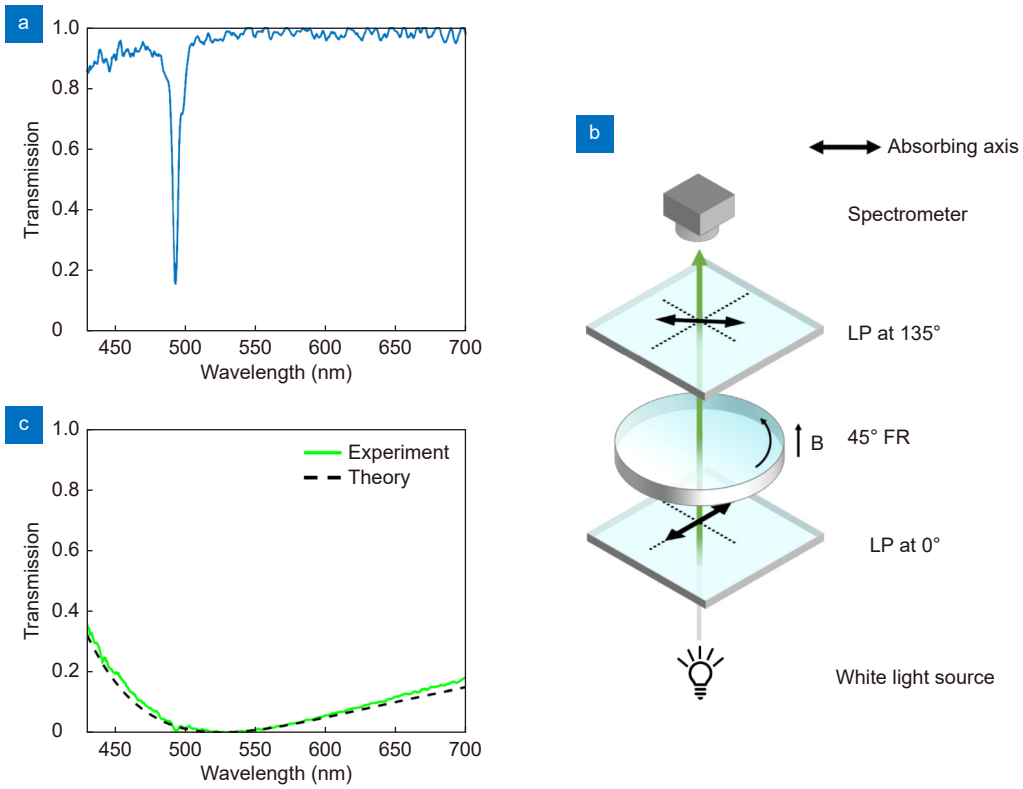

Fig. 5 | Characterization of the FR in the novel pancake optics system. (**a**) Transmission spectrum of the FR. (**b**) Measurement setup for characterizing polarization rotation. LP stands for linear polarizer. (**c**) Measured and calculated normalized transmission spectra (zero means perfect polarization rotation) of the FR.

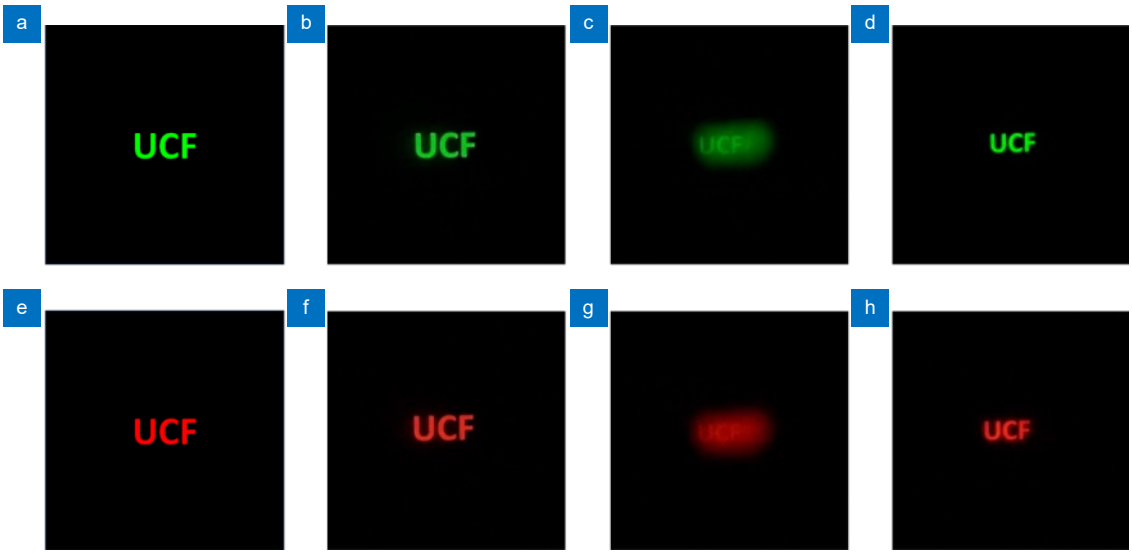

Fig. 6 | 5Experiments using a micro-OLED panel. (**a**) Original image. (**b**) 0th order folded image and (**c**) 1st order image in the pancake system without a FR. (**d**) 1st order image in the pancake system with a FR operating in 510-550 nm. (**e**) Original image. (**f**) 0th order folded image and (**g**) 1st order image in the pancake system without a FR. (**h**) 1st order image in the pancake system with a FR operating in 603–663 nm.

1.43% of the light will leak out and become a ghost image when it interacts with the second RP for the first time. However, this ghost image is not at the same focal plane as the signal image, making it barely visible in Fig. 6(d). To clearly capture the ghost, we switch the focal plane from the signal to the ghost image. As shown in Fig. 7(b), we find that there is a weak ghost image "UCF" behind a blurry image (out-of-focus signal image). Fortunately, the polarization state of this ghost image is orthogonal to that of the signal. To eliminate such a ghost

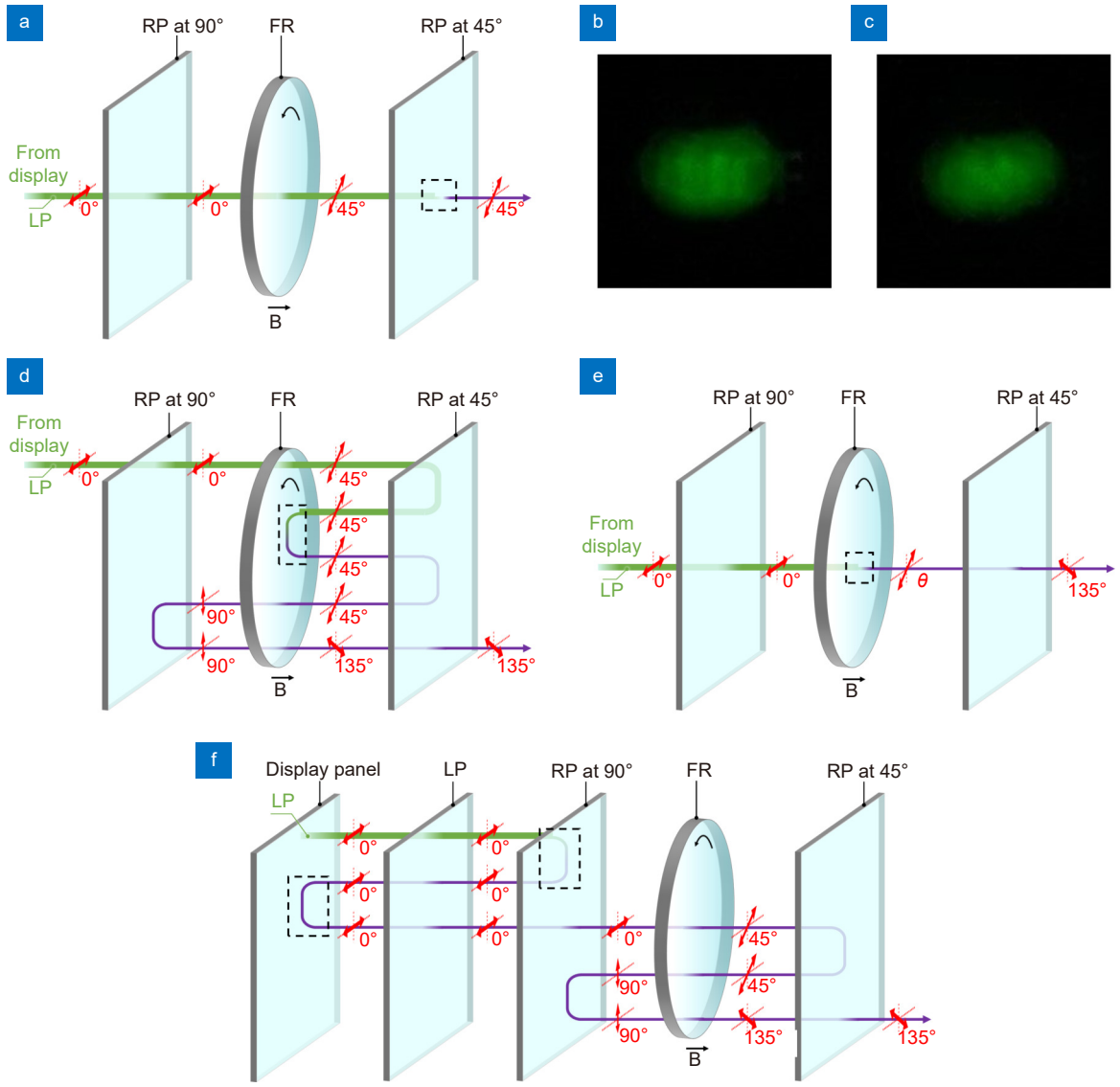

Fig. 7 | Mechanism of ghost images in the novel pancake optics system. (**a**) Light path of ghost images generated by the transmission of the RPs in block state. (**b**) Ghost images (**c**) and suppressed ghost images by an extra linear polarizer captured at its own focal plane. (**d**) Light path of ghost images caused by surface reflection of FR. (**e**) Light path of ghost images produced from imperfect polarization rotation in FR. (**f**) Light path of ghost images induced by panel reflection and reflection of the RPs in transmission state.

image, we can use an absorptive sheet linear polarizer. The image in Fig. 7(c) was captured after applying a linear polarizer. We find that the weak ghost image "UCF" has vanished and only the blurry image (out-of-focus signal image) remains. However, the linear polarizer also absorbs the pass state. Therefore, the most effective solution is to replace the employed DBEF reflective polarizers with an RP having a lower transmission in the block state, e.g., 0.1%.

The second type of ghost images is mainly caused by the surface reflections from the FR, which account for approximately 1% of the light. As illustrated in Fig. 7(d), when the light encounters the FR, around 0.76% of it will be reflected, undergoing multiple folds inside the pancake system, and eventually leaking out as a ghost image. A similar ghost image is generated when the light encounters the FR for the third time. Applying an antireflection coating to the FR can reduce these ghost images. Compared to the signal image, this type of ghost image is very weak and is hardly captured by our camera. This analysis can also be applied to lens surfaces.

The third type of ghost images primarily stems from imperfect polarization rotation in the FR, especially at a large incident angle and a broadband light source. As described in Fig. 7(e), if the polarization state rotates by θ (e.g., 40°) instead of the designed angle, 45°, then

approximately 0.62% of the light will transform into ghost image. This process generates another ghost image when the light encounters the FR for the third time. Using a broadband FR helps minimize this type of ghost image.

The fourth type of ghost images mainly results from the combination of surface reflections from the micro-OLED panel and other undesired processes, such as the high reflection (8%) of DBEF RPs in the pass state and reflections from the panel itself. As illustrated in Fig. 7(f), some of the light is reflected as it encounters the first RP. Subsequently, the light passes through a linear polarizer, reflects off the micro-OLED, passes through the linear polarizer again, undergoes the same folding process as the signal image, and becomes ghost images. Using an RP with a lower reflection in the pass state greatly suppresses these ghost images. In addition, when combined panel reflection, surface reflection from FR, and imperfect polarization rotation will generate similar ghost images. This type of ghost image can be significantly reduced by replacing the linear polarizer with a circular polarizer.

In summary, for the RPs, maintaining high reflection in the block state and high transmission in the pass state is crucial for preserving system efficiency. Also, ensuring a low transmission in the block state and low reflection in the pass state helps reduce light leakage in the system, ultimately minimizing the occurrence of ghosts and enhancing the image contrast[26]. Controlling the polarization state throughout the entire optical path is essential. Another critical component is the FR, which is responsible for managing the polarization rotation within the system. To achieve an optimal performance, the FR should be transparent and achromatic across the designed wavelength range. This not only improves system efficiency but also reduces the presence of ghosts by maintaining the correct polarization states.

To investigate the color performance of our proposed system, a white image is displayed on the micro-OLED in our pancake optics system. The captured images are

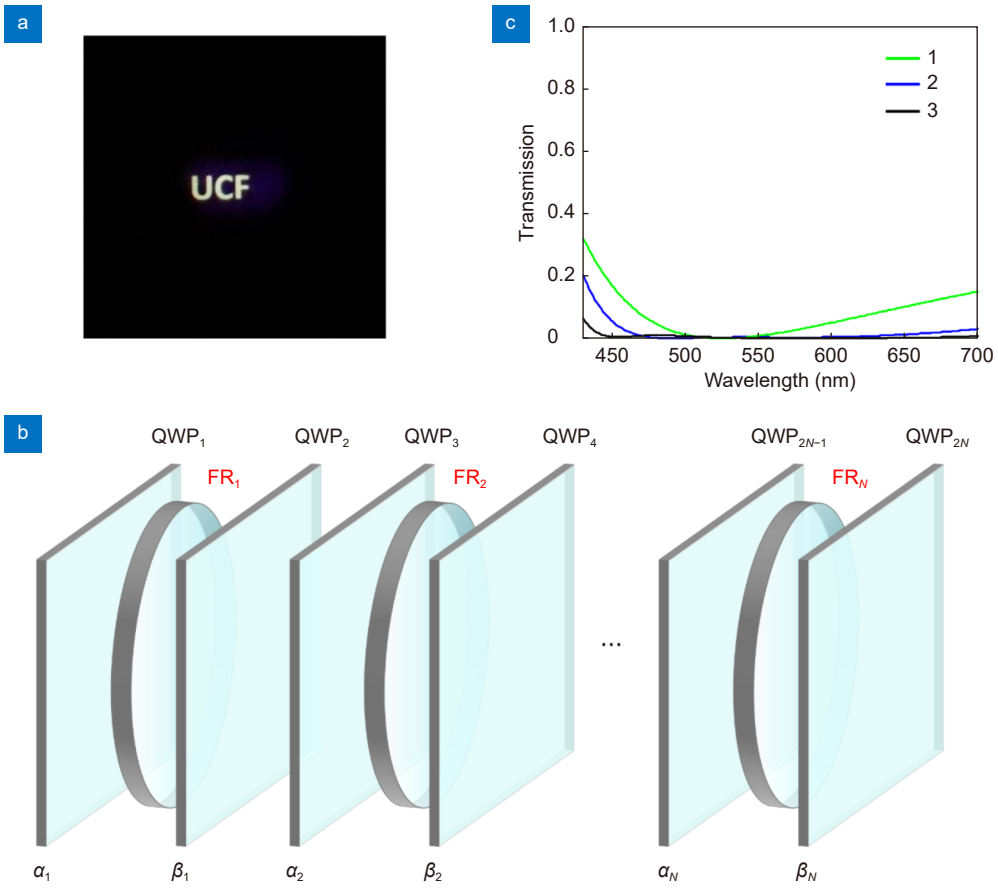

Fig. 8 | Achieving broadband FR. (**a**) 1st order white image in the pancake system with a FR operating in 510-550 nm. (**b**) Broadband FR design of sequences of FRs and QWPs. (**c**) Spectrum of polarization rotation ability using a single piece FR, two sequences of FRs and QWPs and three sequences of FRs and QWPs.

presented in Fig. 8(a), where the white image represents the signal, and the purple image (very dim) corresponds to the ghost image. The ghost image is significantly stronger than the previous one due to the inadequate bandwidth, as Fig. 5(c) shows, of the employed Faraday rotator. Since the Faraday rotation is a result of circular birefringence, the rotation angle is wavelength dependent. For instance, the dispersion of the Verdet constant of the TGG crystal can be described using following equation[25]:

$$V(\lambda) = \frac{K}{\lambda_0^2 - \lambda^2}\ , \tag{2}$$

where K=4.45 * 10^7 radnm^{2}T^{-1}m^{-1} and $\lambda_0 = 258.2$ nm is the effective transition wavelength. TGG is a promising FR material in the 400–1100 nm range, except for an absorption band in the 470–500 nm region. Such an absorption band may absorb a small portion of the blue LED because its major absorption wavelength occurs at 490 nm as shown in Fig. 5(c). Besides, other materials like CeF_3, can completely replace TGG crystal without absorption because CeF_3 exhibits a similar Verdet constant to TGG, but with a much higher transmittance in the whole visible region[28].

For most FR materials, their Verdet constant decreases (in absolute value) with increasing wavelength: for TGG it is equal to 206 radT^{-1}m^{-1} at 532 nm and 134 radT^{-1}m^{-1} at 632 nm. This is the reason that FR works only for a narrow range of wavelengths. However, to make the proposed pancake system for full color images, a broadband FR is required. To achieve a broadband FR, a common method is to compensate the dispersion of FR using a reciprocal polarization rotator[29]. However, this method can only realize broadband FR in one direction. To further broaden the spectral response of FR in both forward and backward directions, the combination of FRs and QWPs is proposed[25]. The proposed system is composed of the sequences of FRs and achromatic QWPs rotated at predetermined angles, as Fig. 8(b) illustrates. More specifically, the process can be expressed by Jones matrix representation. When the light propagates in the forward direction through only one sequence of the system, the output light will have the form:

$$\begin{aligned} \boldsymbol{J}_{\rm o} =& \boldsymbol{R}_{\rm f} * \boldsymbol{J}_{\rm i} = \boldsymbol{R}(-\beta) * \boldsymbol{WP}(\pi/2) * \boldsymbol{R}(\beta) * \boldsymbol{R}(\theta) \\ & * \boldsymbol{R}(-\alpha) * \boldsymbol{WP}(\pi/2) * \boldsymbol{R}(\alpha) * \boldsymbol{J}_{\rm i}\ , \end{aligned} \tag{3}$$

where $\boldsymbol{J}_{\rm i}$ and $\boldsymbol{J}_{\rm o}$ are the Jones vector of input and output light, $\boldsymbol{R}_{\rm f}$ indicates the Jones matrix of a sequence of FR and QWPs in the forward propagation, $\boldsymbol{R}$ represents the rotation matrix, $\boldsymbol{WP}(\pi/2)$ corresponds to the phase retardation matrix of a QWP, θ is the rotation angle of the FR, and α and β are the azimuthal angles of the two QWPs, respectively. For backward propagation, the process is described as follows:

$$\begin{aligned} \boldsymbol{J}_{\rm o} =& \boldsymbol{R}_{\rm b} * \boldsymbol{J}_{\rm i} = \boldsymbol{R}(-\alpha) * \boldsymbol{WP}(\pi/2) * \boldsymbol{R}(\alpha) \\ & * \boldsymbol{R}(\theta) * \boldsymbol{R}(-\beta) * \boldsymbol{WP}(\pi/2) * \boldsymbol{R}(\beta) * \boldsymbol{J}_{\rm i}\ , \end{aligned} \tag{4}$$

where $\boldsymbol{R}_{\rm b}$ indicates the Jones matrix of a sequence of FR and QWPs in the backward propagation. For the multiple sequences of FRs and QWPs, the output light can be expressed as $\boldsymbol{J}_{\rm o} = \boldsymbol{R}_{\rm bN} * \cdots * \boldsymbol{R}_{\rm b2} * \boldsymbol{R}_{\rm b1} * \boldsymbol{J}_{\rm i}$ in the forward propagation, whereas for backward propagation, it has the form as $\boldsymbol{J}_{\rm o} = \boldsymbol{R}_{\rm b1} * \boldsymbol{R}_{\rm b2} * \cdots * \boldsymbol{R}_{\rm bN} * \boldsymbol{J}_{\rm i}$.

Here, we initially try to achieve a broadband FR with two sequences of FRs and QWPs, each with the Faraday rotation θ_k and QWPs rotated at angles α_k and β_k with respect to their fast polarization axes. After optimization based on the Jones matrix representation in Eq. (3) and Eq. (4), a broadband spectrum is achieved for two sequences of FRs and QWPs at rotation angles $\theta_1 = 40.9°$, $\theta_2 = 80.4°$, $\alpha_1 = 93°$, $\beta_1 = 89.6°$, $\alpha_2 = 52.1°$, and $\beta_2 = 13.4°$. Here, the designed central wavelength of each FR is 525 nm. However, the spectral bandwidth is still not broad enough in the visible region. To further broaden the spectral response, three sequences of FRs and QWPs are employed. After optimization, a broader spectrum is realized at rotation angles $\theta_1 = 79.6°$, $\theta_2 = 85.6°$, $\theta_3 = 42.1°$, $\alpha_1 = 87.7°$, $\beta_1 = 80.5°$, $\alpha_2 = 141.2°$, $\beta_2 = 45.3°$, $\alpha_3 = 161.5°$, and $\beta_3 = 139.5°$. Compared to a single FR, the bandwidth is dramatically broadened by the above method as illustrated in Fig. 8(c).

To successfully apply our proposed pancake optics system to near-eye displays, there is an urgent need for a thin-film Faraday rotator operating in the visible region. The FR used in our experiments is made of TGG crystal, which has a very low absorption and a relatively large Verdet constant in the visible spectral region. However, the Verdet constant of TGG crystal is still too small to provide the desired 45° polarization rotation angle in a thin film. Considerable research has been conducted in the past on materials with large Verdet constants[30,31]. For example, a recent research[32] has unveiled a class of organic materials with a giant Verdet constant of nearly 8×10^4 radT^{-1}m^{-1} at around 520 nm. This Verdet constant is approximately 360× larger than that of TGG crystal, implying that a thin film made from such a ma-

terial could be 360× thinner than TGG. Additionally, the effective aperture of the commercial TGG crystal is too small, only around 5 mm, because of the fringe field effect of external magnets. Such a small effective aperture will undoubtedly lead to a relatively small FoV. Therefore, the source of magnetic field plays a crucial role. As mentioned earlier, the magnetic field for the FR can be generated by a solenoid, external magnets, or from the magnetized material itself. The first two approaches could be too bulky and heavy to support a large FoV for a compact and lightweight VR headset. Clearly, the preferred FR should be a magnetless thin film having a large effective area[33,34]. Indeed, thin films [20 mm × 20 mm × 480 μm] of magnetization latching bismuth-substituted rare-earth iron garnets (BIG) have been produced from commercially available materials by mechanical lapping, dice polishing, and crystal-ion-slicing or by adjusting the incorporation of europium[35]. Such a material is grown on the (111)-oriented single crystal Ca/Mg/Zr-substituted gadolinium gallium garnet substrates. As grown, its magnetization axis is normal to the plane of the film, thus achieving a magnetless FR. Currently, magnetless FRs are commercially available from Coherent. However, the BIG Faraday rotator is primarily operated in the near-infrared region (e.g., λ=1.55 μm) due to its strong absorption in the visible region. Therefore, our demonstrated novel pancake optics with a thin-film BIG Faraday rotator should be feasible for some near-infrared imaging applications. To extend the novel pancake optics to commercial VR headsets, the urgent demand for a thin-film Faraday rotator that is magnetless and highly transparent, while possessing a large Verdet constant in the visible region, will stimulate future material developments.

Conclusion

We have proposed and demonstrated a novel pancake optics system using a nonreciprocal polarization rotator sandwiched between two reflective polarizers, which can overcome the efficiency limitations of traditional pancake optics systems. Our measured optical efficiency is 71.5%, which is ~5% lower than the calculated value. By further applying antireflection coating to the optical components and using a better-quality RP, we can raise the optical efficiency to about 93.2%. Additionally, we have investigated four types of ghost images in this system and provided corresponding methods to mitigate or eliminate them. Furthermore, to achieve a full-color display, we proposed to use a multi-layer FRs to achieve broadband operation. Overall, these demonstrations showcase the potential that the novel pancake optics system can revolutionize next-generation VR displays with lightweight, compact formfactor, and low power consumption. Besides, the pressing need for a thin-film FR that is both magnetless and highly transparent, while possessing a large Verdet constant in the visible region, is expected to inspire the next-round magneto-optic material development in the future.

References

1. Kress BC. *Optical Architectures for Augmented-, Virtual-, and Mixed-Reality Headsets*. (SPIE, Bellingham, Washington, 2020).
2. Xiong JH, Hsiang EL, He ZQ, Zhan T, Wu ST. Augmented reality and virtual reality displays: emerging technologies and future perspectives. *Light Sci Appl* **10**, 216 (2021).
3. Yin K, Hsiang EL, Zou JY, Li YNQ, Yang ZY et al. Advanced liquid crystal devices for augmented reality and virtual reality displays: principles and applications. *Light Sci Appl* **11**, 161 (2022).
4. Lu YQ, Li Y. Planar liquid crystal polarization optics for near-eye displays. *Light Sci Appl* **10**, 122 (2021).
5. Ding, Y. et al. Waveguide-based augmented reality displays: perspectives and challenges. *eLight* **3**, 24 (2023).
6. Chang CL, Bang K, Wetzstein G, Lee B, Gao L. Toward the next-generation VR/AR optics: a review of holographic near-eye displays from a human-centric perspective. *Optica* **7**, 1563–1578 (2020).
7. Park HS, Hoskinson R, Abdollahi H, Stoeber B. Compact near-eye display system using a superlens-based microlens array magnifier. *Opt Express* **23**, 30618–30633 (2015).
8. Xiong JH, Wu ST. Planar liquid crystal polarization optics for augmented reality and virtual reality: from fundamentals to applications. *eLight* **1**, 3 (2021).
9. Yang X, Lin Y, Wu TZ, Yan ZJ, Chen Z et al. An overview on the principle of inkjet printing technique and its application in microdisplay for augmented/virtual realities. *Opto-Electron Adv* **5**, 210123 (2022).
10. Li, Y. et al. Metasurfaces for near-eye display applications. *Opto-Electron Sci* **2**, 230025 (2023).
11. LaRussa JA, Gill AT. The holographic pancake window TM. *Proc SPIE* **162**, 120–129 (1978).
12. Wong TL, Yun ZS, Ambur G, Etter J. Folded optics with birefringent reflective polarizers. *Proc SPIE* **10335**, 103350E (2017).
13. Geng Y, Jacques G, Brian W, Peng FL, Yusufu S et al. Viewing optics for immersive near-eye displays: pupil swim/size and weight/stray light. *Proc SPIE* **10676**, 1067606 (2018).
14. Li YNQ, Zhan T, Yang ZY, Xu C, Likamwa PL et al. Broadband cholesteric liquid crystal lens for chromatic aberration correction in catadioptric virtual reality optics. *Opt Express* **29**, 6011–6020 (2021).
15. Le J, Hao B, Aastuen D, Kent S, Kotz A et al. High resolution reflective polarizer lens for catadioptric VR optics with accommodating eye box design. *Proc SPIE* **12449**, 124490O (2023).
16. Zou JY, Zhan T, Hsiang EL, Du XP, Yu XM et al. Doubling the optical efficiency of VR systems with a directional backlight and a diffractive deflection film. *Opt Express* **29**, 20673–20686

(2021).
17. Hsiang EL, Yang ZY, Zhan T, Zou JY, Akimoto H et al. Optimizing the display performance for virtual reality systems. *OSA Continuum* **4**, 3052–3067 (2021).
18. Qian Y, Yang Z, Huang YH et al. Directional high-efficiency nanowire LEDs with reduced angular color shift for AR and VR displays. *Opto-Electron Sci* **1**, 220021 (2022).
19. Wu YH, Tsai CH, Wu YH, Cherng YS, Tai MJ et al. 5-2: *Invited paper*: high dynamic range 2117-ppi LCD for VR displays. *SID Symp Dig Tech Pap* **54**, 36–39 (2023).
20. Komura S, Okuda K, Kijima H. 49-4: thin and lightweight head-mounted displays with polarized laser backlights and holographic optics. *SID Symp Dig Tech Pap* **53**, 636–639 (2022).
21. Luo ZY, Ding YQ, Rao Y, Wu ST. High-efficiency folded optics for near-eye displays. *J Soc Inf Display* **31**, 336–343 (2023).
22. Usukura N, Minoura K, Maruyama R. Novel pancake-based HMD optics to improve light efficiency. *J Soc Inf Display* **31**, 344–354 (2023).
23. Saleh BEA, Teich MC. *Fundamentals of Photonics*, *Multi-Volume* 3rd ed (John Wiley & Sons, Hoboken, 2019).
24. Inoue M, Levy M, Baryshev AV. *Magnetophotonics*: *From Theory to Applications* (Springer, Berlin, 2013).
25. Berent M, Rangelov AA, Vitanov NV. Broadband Faraday isolator. *J Opt Soc Am A* **30**, 149–153 (2013).
26. Hou QC, Cheng DW, Li Y, Zhang T, Li DY et al. Stray light analysis and suppression method of a pancake virtual reality head-mounted display. *Opt Express* **30**, 44918–44932 (2022).
27. Cheng DW, Cheng DW, Cheng DW, Hou QC, Li Y et al. Optical design and pupil swim analysis of a compact, large EPD and immersive VR head mounted display. *Opt Express* **30**, 6584–6602 (2022).
28. Zhang ZH, Wu Z, Zhang Z, Su LB, Wu AH et al. Characteristics and recent development of fluoride magneto-optical crystals. *Magnetochemistry* **9**, 41 (2023).
29. Schulz PA. Wavelength independent Faraday isolator. *Appl Opt* **28**, 4458–4464 (1989).
30. Nelson Z, Delage-Laurin L, Swager TM. ABCs of faraday rotation in organic materials. *J Am Chem Soc* **144**, 11912–11926 (2022).
31. Carothers KJ, Norwood RA, Pyun J. High Verdet constant materials for magneto-optical faraday rotation: a review. *Chem Mater* **34**, 2531–2544 (2022).
32. Vandendriessche S, Van Cleuvenbergen S, Willot P, Hennrich G, Srebro M et al. Giant faraday rotation in mesogenic organic molecules. *Chem Mater* **25**, 1139–1143 (2013).
33. Levy M. Nanomagnetic route to bias-magnet-free, on-chip Faraday rotators. *J Opt Soc Am B* **22**, 254–260 (2005).
34. Karki D, Stenger V, Pollick A, Levy M. Thin-film magnetless Faraday rotators for compact heterogeneous integrated optical isolators. *J Appl Phys* **121**, 233101 (2017).
35. Abbott RR, Fratello VJ, Licht SJ, Mnushkina I. Article comprising a faraday rotator that does not require a bias magnet. Patent 6770223 (2004).

Acknowledgements

The UCF group is indebted to Dr. Yu-Hsin Huang of AUO Corporation for providing the DBEF films.

Author contributions

Y. Q. Ding proposed the idea and initiated the project. Y. Q. Ding mainly conducted the experiments and simulations and wrote the manuscript. Z. Y. Luo helped with experiments and G. Borjigin helped with simulations. S. T. Wu supervised the project and S. T. Wu edited the manuscript.

Competing interests

The authors declare no competing financial interests.

Scan for Article PDF